Article:
Taras, P., Li, G., Zhu, Z.Q. et al. (2019) Combined multi-physics model of switched flux PM machines under fault operations. IEEE Transactions on Industrial Electronics, 66 (9). pp. 6737-6745. ISSN: 0278-0046

https://doi.org/10.1109/TIE.2018.2877089

Combined Multi-Physics Model of Switched Flux PM Machines under Fault Operations

P. Taras, G. J. Li, *Senior Member, IEEE*, Z. Q. Zhu, *Fellow, IEEE*, M. P. Foster, and D. A. Stone

***Abstract*—In this paper, the transient thermal response of a conventional double layer switched flux permanent magnet machine is studied for both healthy and fault conditions such as inter-turn short-circuit. A highly optimized and accurate co-simulation model for different operating conditions is developed requiring low computation and time resources. The electro-mechanical models for both healthy and faulty operation are implemented in Matlab/Simulink while the thermal model is implemented using 3D FEM software. Both models are dynamically coupled to enable the influence of temperature rise on the electromagnetic performance and vice versa to be predicted. Operation under various conditions are investigated and it is found that the temperature rise under fault conditions and high speed can lead to irreversible demagnetization of the permanent magnets. The superposition principle is used to accurately estimate the impact of short-circuit currents on the temperature rise. A series of dynamic tests are carried out to validate the transient thermal response prediction when operating during both the healthy and fault conditions.**

***Index Terms*—Demagnetization, fault tolerant control, permanent magnet motors, short-circuit currents, thermal analysis.**

I. INTRODUCTION

THERMAL design is crucial when developing new products with a high power to mass (or volume) ratio constraint like the electrical machines used in the aircraft or automotive industries. The challenges involved achieving a suitable solution are multiple and sometimes exclusive. For example, permanent magnets (PMs) are well-known to achieve a high power density, however, their performance and operational status largely depend on temperature rise. At high speeds, both the eddy current loss within the PMs and the iron losses in the adjacent laminated iron core are high, leading to potential temperature rise with disastrous consequences like irreversible demagnetization. Another demanding requirement is capability of functioning for a limited time interval in a so called degraded mode, i.e. operating with reduced torque and/or speed, or operating with increased torque ripple, etc. These operating features are essential for safety-critical applications but the presence of a fault where, for example, an inter-turn short-circuit in one of the windings can push the working temperature of the machine to an unacceptable level. To allow operation under elevated temperatures that can occur under fault condition, detailed thermal analysis often needs to be carried out during the design phase [1] focusing on topics such as additional cooling, structure optimization, material choice and also proper topology selection.

A promising candidate for the aircraft and automotive applications is the switched flux permanent magnet machine (SFPMM) which is a novel topology providing high torque density and robust rotor construction [2], [3], [4], [5]. Compared with rotor-mounted PM synchronous machines, the SFPMM improves on several aspects, [6], [7]. Both PMs and windings are located on the stator, as shown in Fig. 1, making them easier to access for cooling. Additionally, the rotor is just a salient iron structure and hence is very robust making it suitable for high speed applications. However, since the PMs are located within the concentrated armature coils they are more exposed to demagnetization resulting from copper losses in the armature windings [8], [9], [10]. Previous studies in [11], [12], [13], [14], [15], [16] have shown remarkable resilience of the SFPMM against irreversible demagnetization at low and medium temperature ranges due to the way in which the PMs are positioned on the flux paths. Further increasing the PM temperature, however, will still result in irreversible demagnetization for the SFPMM. Although important, the issue of thermal analysis in the SFPMMs has been brought under investigation only recently and most of previous investigations are focused on the electromagnetic finite element (FEM) models [11], [12], [13], [14]. In these models, the PM material is assumed to be working at an imposed temperature while the machine operates in healthy mode. While this approach has the advantage of using simpler models, it does not give full information about the thermal response of the machine or its behavior under fault conditions. Recent work has been reported in [15], [16] applying this technique to certain short circuit fault conditions assuming temperatures up to 150°C, however, without thorough thermal analysis one cannot be certain if high value of temperature is a true reflection of the loss mechanisms. Only in [17] and [18] was a transient thermal analysis conducted for SFPMM working under healthy conditions and in generator mode. This work assumed constant copper and iron losses, thus offering limited insight into machine operation. In [19] a coupled model is implemented for healthy conditions, based on improved 2D FEM models. Although the authors suggest a faster simulation time, they limit the study to steady-state thermal performance assessment. Finally, in [20] a multi-physics (thermal-electromagnetic) model considering faulty conditions is investigated for the SFPMM. The electro-mechanical domain is implemented in Matlab/Simulink while the thermal domain is a 3D FEM model or alternatively based on lumped parameter networks but it does not provide bi-directional coupling. Specifically, the heating sources are generated in the electromechanical model

and carried over into the thermal one. However, the calculated temperatures in the thermal model are not fed back to the electromechanical model. So this kind of model is often unidirectional, and most time the machine is operating at one single working point (constant torque and speed).

This paper describes a comprehensive model of a SFPMM providing full bidirectional coupling between the electromechanical and thermal domains. By combining Matlab/Simulink with 3D FEM a temperature dependent model is developed suitable for simulating accurately a multitude of operating conditions and characteristics thereby addressing some of the limitations previously described in literature. The model allows the study of both the healthy and faulty operations as well as the influence of various parameters (like speed) on the temperature rise and vice versa. Using this coupled model, the influence of temperature and also short-circuit current on the magnet demagnetization has been comprehensively investigated. Moreover, the control strategy effect can also be taken into account.

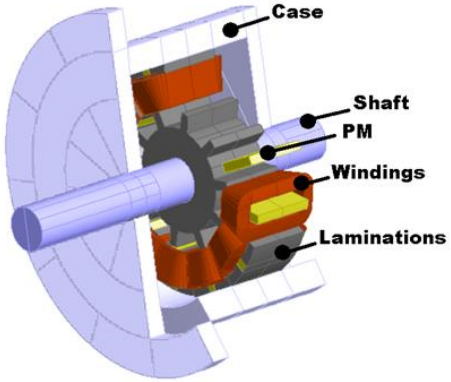

Fig. 1. 3D view of the considered SFPMM.

II. The Co-Simulation Model

A. Investigation Methodology

The 3D view of the modeled SFPMM is shown in Fig. 1 while the main parameters are given in Table I. The employed PM material is NdFeB (N35M grade).

TABLE I
PARAMETERS OF THE INVESTIGATED MACHINES

Stator slot number	12	Stator yoke height (mm)	3.6
Rotor pole number	10	Stack length (mm)	25
Rated speed (rpm)	400	Air-gap length (mm)	0.5
Rated rms current (A)	11	Rotor outer radius (mm)	27.5
Rated torque (Nm)	2.2	Magnet thickness (mm)	3.6
Stator outer radius (mm)	45	Remanence (NdFeB) (T)	1.2
Stator inner radius (mm)	28	Number of turns/phase	72

The proposed co-simulation model combines a Matlab/Simulink (electro-mechanical domain) component with a 3D FEM thermal one, as shown in Fig. 2. The electromechanical domain model explicitly includes temperature dependent parameters (such as material B-H characteristics) which are able to be influenced by the outputs of the thermal FEA calculation step. Thus, the electromagnetic performance under fault or healthy conditions obtained by electromagnetic and mechanical models (Matlab/Simulink) will influence the temperature obtained in the thermal model, and the temperature will be fed back to the electromagnetic model like a closed loop, which will predict the temperature dependent performance such as EMF, cogging torque, on-load torque and losses, particularly the copper losses. The variation in losses will again influence the temperature within electrical machines. These iterations of calculations based on the bi-directionally coupled model allow us to actually predict the temperature variations and also its influence on the electromagnetic performance under healthy and fault conditions.

The main challenge in building a general model capable of accounting for coupled electromagnetic-thermal phenomena and also faulty operations is accounting for the effects of the time constants between the two domains. This is mainly due to the necessity of using a small time step (~ms) in the electromechanic domain in order to achieve acceptable accuracy. However a much larger time constant (~hours) is required for the thermal domain modelling. The simulated operation time of the multi-physics model is necessarily long as the response is dominated by the dynamics of the thermal model, however, to accurately represent the electromechanical domain the simulation must be run using much shorter time steps. This is very computationally demanding and requires particular attention.

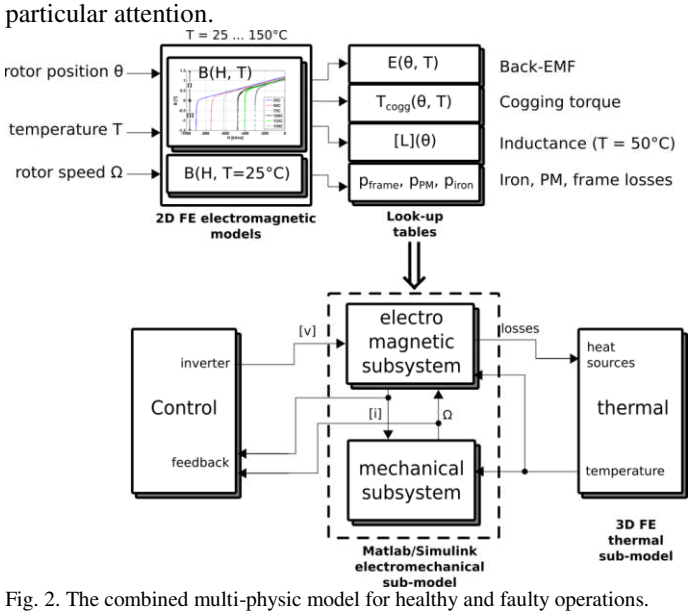

Fig. 2. The combined multi-physic model for healthy and faulty operations.

B. Electromechanical Model and Associated Control

The aforementioned SFPMM works under the classic speed control strategy, as shown in Fig. 3. The Matlab/Simulink model is based on the voltage and torque equations (7) and (8) in the Appendix.

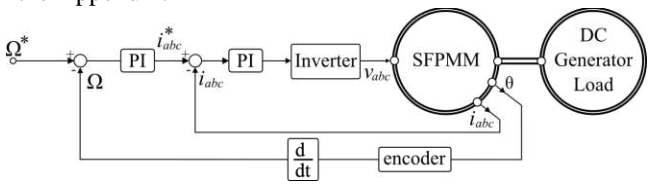

Fig. 3. The block diagram with current and speed controls.

By way of an example, Fig. 4 shows a fault operating condition where for phase A, one coil (A1) out of a total of four

coils is affected by a short-circuit, i.e. 25% fault severity.

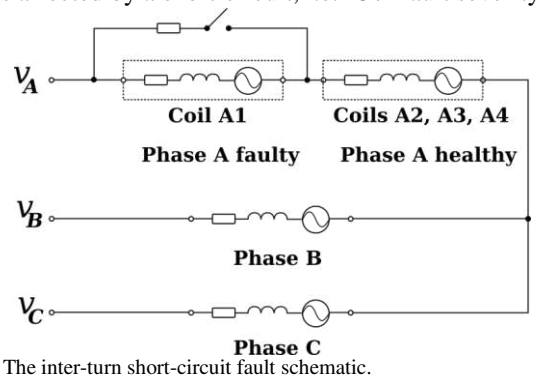

Fig. 4. The inter-turn short-circuit fault schematic.

The electro-mechanical model computes the heat sources (copper loss, iron losses and PM eddy current loss) which are going to be used later in the thermal model. The iron losses (calculated using the method introduced in [21]), the PM and frame losses are implemented in look-up tables. To reduce the model complexity, the PM eddy losses are assumed to be independent of the temperature variation and only dependent on the speed, as shown in Fig. 5. The FEM results have shown that the PM losses at 150° C decrease by only 9% when compared with the 25° C case, which justifies the above simplification. However, the copper losses depend on the computed current and the phase resistance, and the latter is temperature dependent.

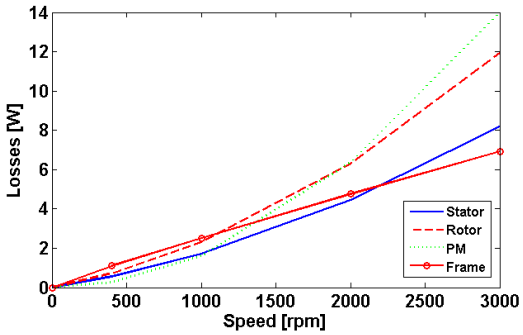

Fig. 5. Stator and rotor iron losses, PM and Frame eddy current losses *vs* rotor speed.

It is worth mentioning that the data exchange between the thermal and electromechanical models is driven by the thermal domain simulation time step and the impact on accuracy is negligible since the electrical quantities vary very slowly with temperature. A variable time step is used for the thermal domain model to cater for a fast transient but lengthy convergence time, with the minimum and maximum time step values set at 25s and 1000s respectively. The electromechanical domain model uses a time step of 0.2ms and so time averaged values for the copper losses are sent as heat source inputs into the thermal domain model.

C. Thermal Domain Model

A 3D FEM thermal model is used in order to account for the effects of the end-winding and end plates as shown in Fig. 6. It is also worth mentioning that the inter-turn short-circuit is studied, which is an asymmetric fault, meaning that the model cannot be reduced based on the available physical symmetries of the machine and the FEM model of the whole machine is necessary.

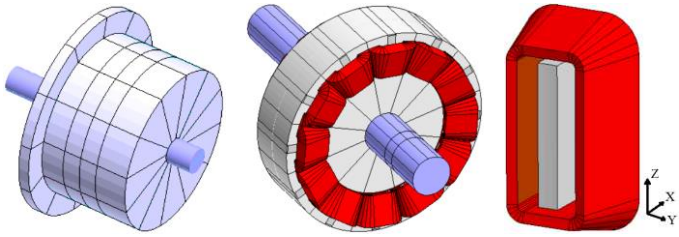

(a) (b) (c)

Fig. 6. The thermal model. (a) Full motor, including end plate, (b) stator and rotor cores, PMs, coils and shaft, (c) single coil surrounding PM.

The thermal properties of the materials used in the model are given in Table II. Concerning the windings, an anisotropic thermal conductivity was considered due to the fact that there is a much stronger heat transfer by conduction in the Z-axis (axial direction) towards the end-windings and not so much in the radial direction, i.e. XY plane, Fig. 6 (c). The radial thermal conductivity is calculated using the method introduced in [22] considering the fact that the fill factor is 0.4 and the winding is not impregnated. The housing is made of aluminum with a polished surface (with an assumed emissivity of 0.09).

TABLE II
THERMAL PROPERTIES OF THE INVESTIGATED MACHINE

Region	Thermal conductivity [W/m/K]	Volumetric Heat Capacity [J/K]
Windings [22]	0.07/0.07/385	1000000
Stator [22]	28/28/0.5	3519000
Rotor	20*	3519000
Frame + Rig	168	2324070
Air	0.0263	1231.1
Shaft	52	3588000

Equivalent* value is calculated using the method introduced in [23].

(1) Airgap heat transfer

Concerning the airgap heat transfer between the stator and rotor, the methodology is to determine first the type of flow (laminar, vortex or turbulent). This is given by Taylor's dimensionless number [24] which was computed for smooth concentric rotating cylinders. However, it was established that with slight modification this can be applied successfully to the slotted rotors and stators for relatively low speed applications, which is the case for this paper. Hence it was decided to treat the salient rotor structure as a constant airgap structure, as shown in Fig. 6 (b), in which the equivalent thermal conductivity of the rotor material was determined using the method introduced in [23]. The Taylor number *Ta* is:

$$Ta = \rho \cdot l_g \cdot \frac{v}{\mu} \cdot \sqrt{\frac{l_g}{R_r}} \qquad (1)$$

where ρ is the air density, l_g is the air-gap radial thickness, R_r is the rotor radius, μ is the air dynamic viscosity and v is the air velocity. For the maximum speed considered (3000 rpm), the *Ta* value is 38.88 which would still allow one to consider the airgap as having a laminar flow. Secondly, based on the *Ta* value, the Nusselt number *Nu* is equal to 2 and allows the determination of the convection coefficient:

$$h = Nu \cdot \frac{k}{L} \tag{2}$$

where k is the air thermal conductivity and L is the characteristic length ($L = 2 \cdot l_g$ for airgap region).

Once the convection coefficient h is calculated, an equivalent thermal conductivity can be obtained in the airgap region, facilitating the 3D FEM thermal model. For simplicity, this approach was also expanded to the end-space regions.

(2) The convection coefficient calculation

The machine housing is cylindrical and is cooled via natural convection. In order to determine the convection coefficient [24], the Grashof and Prandtl dimensionless numbers are determined first. The Grashof number (Gr) is defined as:

$$Gr = \beta \cdot g \cdot \Delta T \cdot \rho^2 \cdot L^3 / \mu^2 \tag{3}$$

where β is the coefficient of cubical expansion $\beta=1/(273+T_{FLUID})$. The T_{FLUID} is the average ambient temperature. ΔT is the difference between the housing external surface temperature and T_{FLUID}. ρ is the air mass density. g is the gravitational acceleration. The characteristic length L is equal to the machine housing diameter. The Prandtl number (Pr) is given by:

$$Pr = c_p \cdot \mu / k \tag{4}$$

where c_p is the air specific heat capacity.

Next the Nusselt number is determined using a correlation for cylindrical objects:

$$Nu = 0.525 \cdot (Gr \cdot Pr)^{0.25} \tag{5}$$

Finally, using the Nusselt number the surface convection coefficients can be determined from (2). The convection coefficient is considered as temperature dependent [25] – more specifically it depends on the surface temperature as illustrated by the Grashof number in (3).

III. Thermal Assessment During the Inter-Turn Short-Circuit

A. Predictions using the Thermal and Electro-Mechanical Models

The thermal transient response is studied for two cases – 400 rpm and 1000 rpm at rated torque and under inter-turn short-circuit condition. The ultimate goal is to estimate the overall temperature rise during the fault operation and to predict if the PMs are in danger of being irreversibly demagnetized. It is worth mentioning that at 400 rpm, the short-circuit current is low (8.5A, peak value) and there is no significant increase in temperature. Therefore, these results were not shown here. However, at 1000 rpm, the potential short-circuit current is high (19.9A, peak value). The considered faulty scenario is such that the machine operates for one hour under healthy conditions, then the short-circuit fault is introduced and the degraded mode maintained by using the control shown in Fig. 3 for the next 1.5 hours. Under these conditions, the solving process of the entire coupled model takes 7 hours on a 2.6 GHz quad core i7 processor computer with 16 Gb RAM and SSD storage. The majority of the time is spent in the electromechanical model due to its small time step.

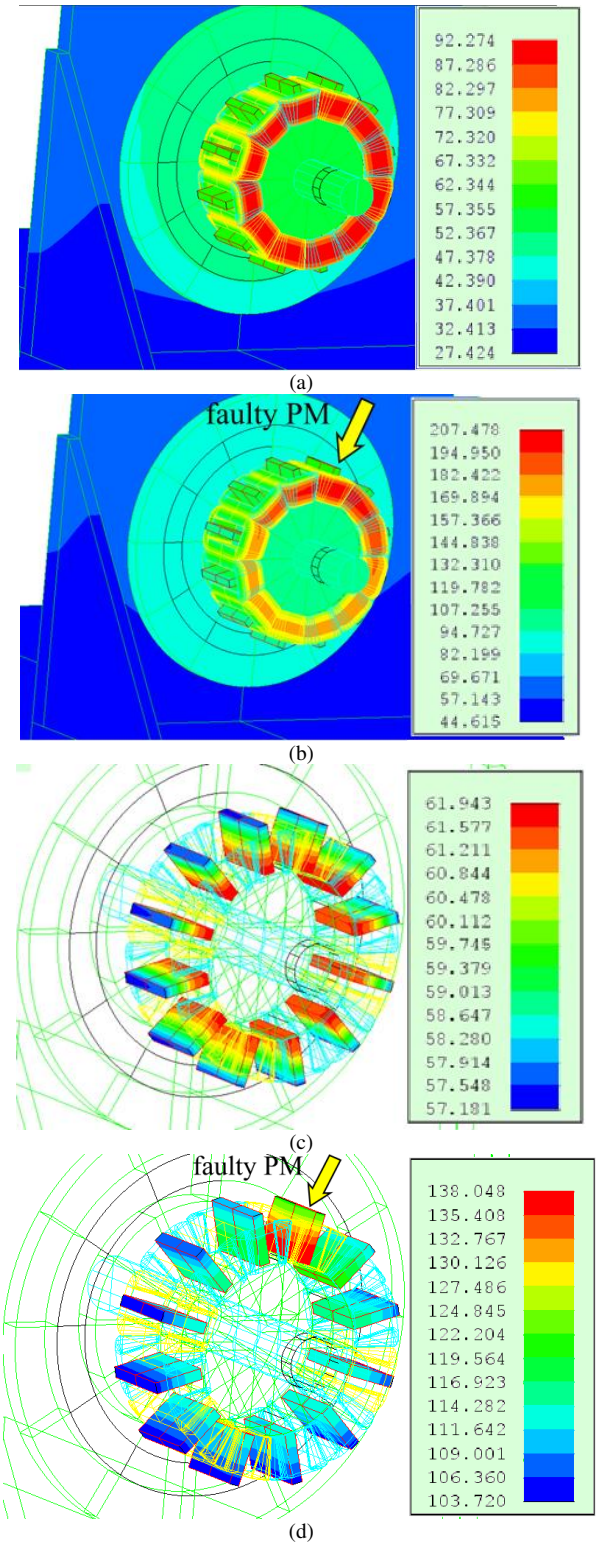

Fig. 7. Temperature distributions within the machine at 1000 rpm. (a) windings (healthy), t = 1 hour, (b) windings (faulty), t = 2.5 hours, (c) PMs (healthy), t = 1 hour, (d) PMs (faulty), t = 2.5 hours. The units in the figures are °C.

The following results are presented for the machine working at 1000 rpm and rated torque (no flux weakening: $I_d = 0$A). The temperature distributions within the machine are shown in Fig.

7. It can be noticed that due to the existing fault there is an imbalance in the temperature distribution for both windings and the surrounded PMs. The affected winding and PM have a temperature rise of 30°C higher than the other the coils and PMs, respectively, contributing to an extra heat source for them. The overall temperature has increased to levels that cause irreversible demagnetization of all PMs. Some PMs, especially the ones far away from the affected coil might only be partially demagnetized. This is because the demagnetization process, while facilitated by the high temperature, does depend on the local magnetic circuit configuration as well, as investigated in [15]. The windings are also subject to temperatures higher than 120°C while reaching a peak of 207°C in the affected coil. This might cause thermal destruction of most of the commercially available insulation materials.

The speed and torque resulting from the electromechanical model are shown in Fig. 8. The temperature has no visible influence over these quantities because the control strategy shown in Fig. 3 compensates them. The speed disturbance due to the inter-turn short-circuit is attenuated in around 10s. However, the torque ripple is high during the faulty mode, as expected.

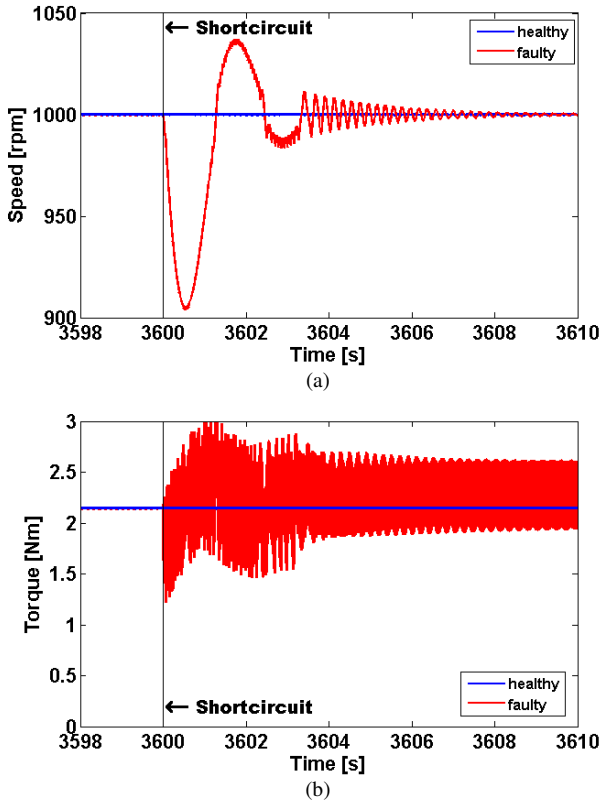

Fig. 8. Speed and torque (1000 rpm, faulty case).

B. *Demagnetization Analysis*

The models studied in the previous sections are analyzed and compared further from the point of view of magnet demagnetization. The first quantities studied are the copper losses, as shown in Fig. 9, which justifies why thermal analysis is necessary. At low speed, the copper losses (only the DC component is considered) in the affected coil have a modest increase of 37% due to the short-circuit fault. The copper losses in the remaining healthy coils (only one representative coil, e.g. B1, is shown) increases with to a similar value due to the fact that the control strategy tries to compensate torque drop due to the fault by increasing the current in the healthy phases. When the fault occurs at a higher speed, e.g. 1000 rpm, the copper losses in the affected coil increase by about 861%, while again the control strategy is responsible for an additional increase of 70% in the healthy coils. These effects need to be correlated to Fig. 5 as the iron, PM and frame losses are also important and can be comparable with the copper losses at high speed. Given the significant copper loss increase during fault operation, it is necessary to investigate the temperature evolution in the machine before and after the fault is introduced.

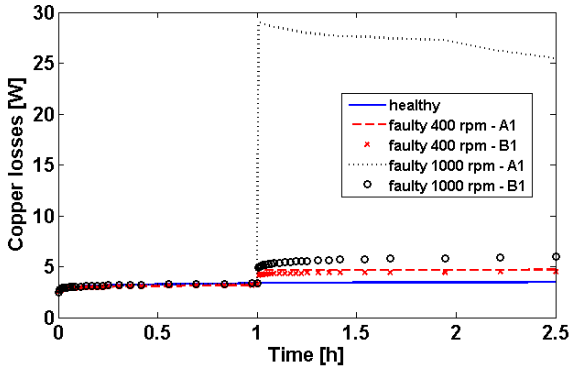

Fig. 9. Copper losses comparison.

The temperature increase in the PMs is studied further, as shown in Fig. 11. Although there are 12 PMs in the machine, only three representative PMs were chosen – the affected PM (A1), the adjacent PM (B1) as well as a third one (A4), located at 90° compared to A1. Fig. 10 shows the locations of the temperature measurement points and the selected PMs.

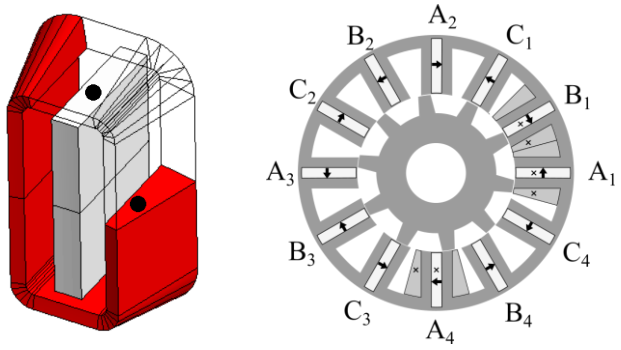

Fig. 10. Locations of thermocouples. (a) single coil and PM – 3D view, (b) all coils and PMs with thermocouples located at A1, B1 and A4.

For the considered PM grade (N35M), 100 °C is the threshold for irreversible demagnetization. It can be noticed that even during normal operation, there is a 7°C (about 10%) increase in temperature for a change in speed from 400 rpm to 1000 rpm due to the higher PM losses. This might justify the necessity of magnet segmentation in order to reduce the PM losses. At rated speed, the temperature in the PMs is still below the irreversible demagnetization threshold. However, at 1000 rpm it can be noticed that all PMs are irreversibly demagnetized within about 30 minutes of the fault being introduced. However, the affected coil's PM demagnetizes in only a couple of

minutes due to the close proximity and coupling to the short-circuited coil.

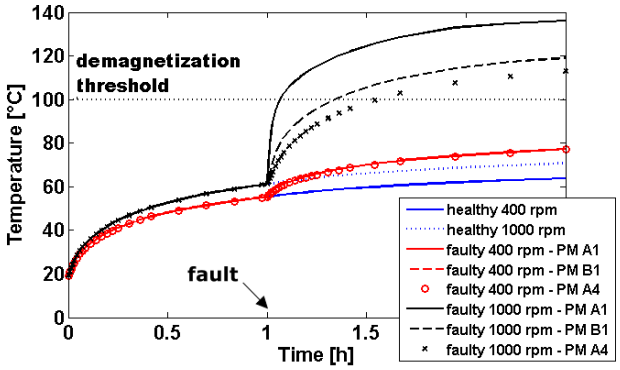

Fig. 11. PM temperature evolution before and after inter-turn short-circuit.

The previous results can be further analysed to assess the influence of the short-circuit current alone on the PM temperature rise. This can be done by applying the superposition principle, which is feasible because the coefficients (thermal conductivity and heat capacity) used in the thermal domain model are linear. The heat source effects can be then separated for regions of interest like the PMs. Two cases are possible considering the heating sources due to winding currents. The first case assumes all coils act as heating sources and are included in the thermal model, which is exactly the same as previous analyses. The second case, however, assumes that the heating source is only due to the short-circuit current in the short-circuited coil and the other coils are open-circuited. Similar to the previous section, the effects of both low and high speeds are considered. The following relation is used to determine the relative temperature rise in PMs or windings during the faulty operation:

$$\Delta T[\%] = \frac{T_{faulty} - T_{healthy}}{T_{healthy} - T_{init}} \cdot 100 \qquad (6)$$

where ΔT is the temperature rise (in %) due to fault mode. $T_{healthy}$ is the temperature achieved during the steady state (2.5 hours) in healthy mode. T_{faulty} is the the steady state temperature in faulty mode. Finally, T_{init} is the initial temperature. Table III summarizes the relative temperature increase during faulty mode based on (6) for the three representative PMs.

TABLE III
TEMPERATURE RISE IN FAULTY MODE*

Region	all coils** 400 rpm	all coils** 1000 rpm	coil A1*** 400 rpm	coil A1*** 1000 rpm
PM A1	29.9 %	127.2 %	24.4 %	104.7 %
PM B1	29.9 %	94.2 %	15.1 %	60.8 %
PM A4	29.9 %	82.1 %	11.8 %	45.2 %

*with respect to the healthy case. **all coils are included. ***only the short-circuited coil is included.

Taking PM A1 as an example, the results in Table III can be interpreted as following. When introducing the fault, the resulting copper losses will produce an increase in temperature by 29.9% (400 rpm) and 127.2% (1000 rpm) with respect to the healthy case. Furthermore, Table III shows the important contribution of the short-circuit current alone to the PM A1 heating. For 400 rpm, the short-circuit current contribute 24.4%/29.9% = 81.6% of PM A1 overheating, and the remaining coils being responsible for less than 20%. This is plausible as the PM A1 is contained in the coil A1. Similar reasoning can be applied for higher speed, showing a contribution of 104.7%/127.2% = 82.3 % of the short-circuit current to total overheating of the PM A1. Extending the analysis to the PM B1 shows 15.1%/29.9% = 50.5% (400 rpm) and 60.8%/94.2% = 64.5% (1000 rpm) contributions due to the short-circuit current in the coil A1. Therefore, there is an important heat flow path from the affected coil (A1) to the adjacent ones during fault conditions.

IV. EXPERIMENTAL VALIDATION OF THERMAL MODEL

A prototype machine was built in order to validate the combined electromagnetic-thermal model considering fault operations, as shown in Fig. 12. However, it was not possible to achieve the filling factor of 0.4 due to the difficulty of winding process – instead a filling factor of 0.35 was achieved for the prototype machine meaning a higher current density is needed to achieve the required rated torque. Therefore, the prototype has a lower thermal load capability, which will be taken into account in the following analyses.

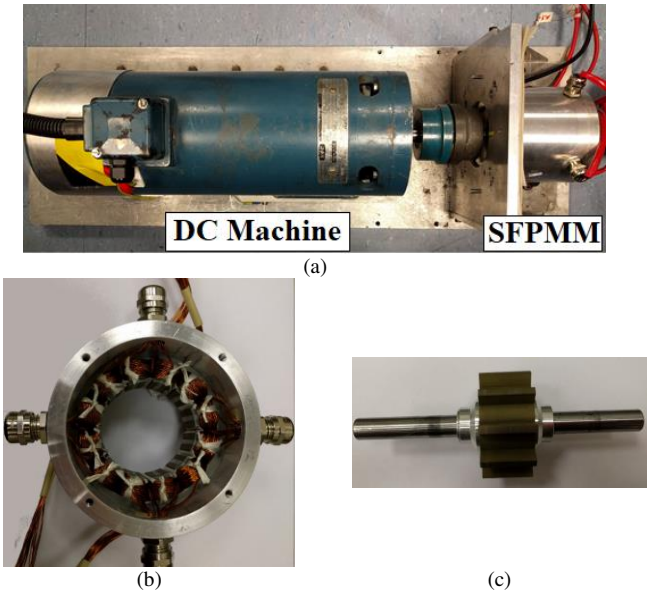

(a)

(b) (c)

Fig. 12. Prototype of SFPMM with 12-slot/10-pole. (a) motor mounted on the test rig with insulation paper, (b) stator, (c) rotor.

In addition, the influence of the test rig was found to be too significant due to the extra surface area of the supporting structure, which might lead to significant overestimation of the thermal performance of the investigated machine. Therefore, several layers of insulation paper (totaling a 0.72 mm) were mounted between the prototype and the rig to limit this influence. There are 7 thermocouples mounted in the machine (Fig. 10) – 3 on windings, 3 on PMs and one on the external surface of the housing. The machine was operated under constant speed control and the temperature is recorded during the dynamic operation. After the machine is stopped, the temperature variation during the cooling down process is also

recorded. In order to remove the noise induced in thermocouples due to the electromagnetic interference (EMI), a thermometer with low pass filter was used.

The results for healthy case are given in Fig. 13. The test conditions are set at rated speed (400 rpm) and a mechanical load equal to 45% of the rated torque. This is necessary to prevent the potential damage due to overheating during the tests. Since the fault is not introduced, the imbalance does not exist, as expected. Therefore, only the temperature variations at three representative locations (coils A1, PM1 and the case) are shown. The predictions correlate well with the experiment measurements since the discrepancy between the predicted and measured results is within 5%.

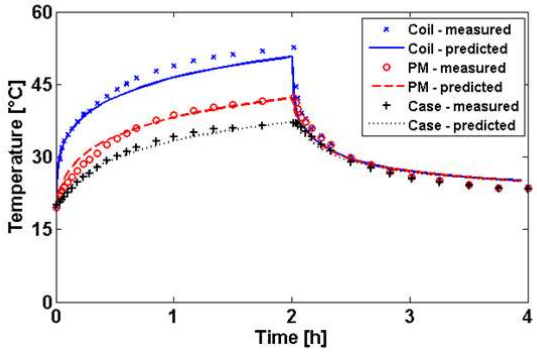

Fig. 13. Temperature variation in healthy case (400 rpm).

For the faulty case, the same conditions are maintained. Introducing the fault shows a noticeable increase in the temperature. This is due to the short-circuit current but also due to the control strategy that increases the currents in the remaining healthy phases to compensate the influence of the short-circuit.

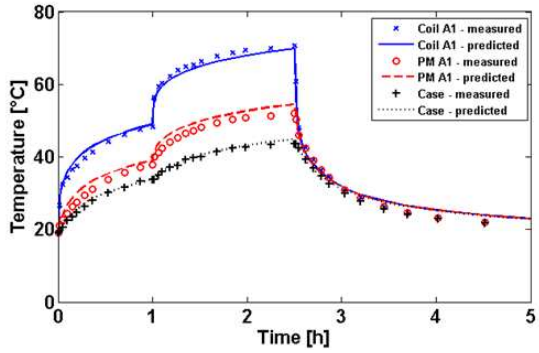

(a)

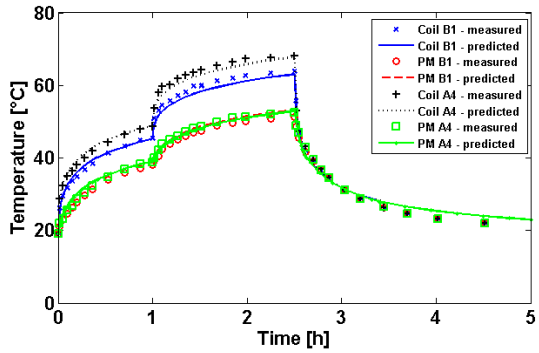

(b)

Fig. 14. Temperature variation in faulty mode. (a) coil A1, PM1, Case, (b) Coils B1 and A4, PM inside B1 and A4.

V. Conclusions

An accurate multi-physics (electromechanical- thermal) model for a SFPMM is proposed in this paper, which can take into account the temperature influence during dynamic operation in either healthy or faulty mode. It reduces the required computation time and resources by implementing the electromechanical part using less demanding Matlab/Simulink models coupled in a bidirectional manner with a 3D FEM thermal model. A key feature is the inclusion of temperature dependent characteristics of various parameters such as back-EMF, cogging torque and phase resistance. Based on this model, an accurate view over the entire process (both healthy and faulty operations) can be obtained and used further in order to develop appropriate fine-tuned fault remedial strategies.

The proposed model is highly recommended as the faults such as inter-turn short-circuit can affect all the PMs, which could be irreversibly demagnetized primarily due to the increase in temperature. In addition, since there is little thermal separation between the coils, the heat generated by the inter-turn short-circuit in one coil can easily spread to other phases causing them to be overheated. The influence of the short-circuit current on temperature rise is quantitatively analyzed, based on the superposition principle. The time needed for the PM to be demagnetized under the inter-turn short-circuit can be assessed accurately.

Based on these conclusions, possible improvements such as the forced convection in the end-winding regions or better overall external cooling might need to be taken into account during design phase for the SFPMM. In addition, iterative thermal design optimizations can be conducted given the reasonable solving time. Further studies concern various fault severities and comparisons with modular SFPMM like C-Core and E-Core topologies are ongoing. These modular machine topologies might provide superior fault tolerant capability due to physical, electromagnetic and thermal separation between phases.

Appendix

The dynamic electro-mechanical model implemented in Matlab/Simulink is based on [23], [26], [27], [28], [29] and can be used for both the healthy and faulty operations:

$$[v] = [R][i] + \frac{d([L][i])}{dt} + [e_0] \tag{7}$$

where $[v]$, $[i]$ and $[e_0]$ are the phase voltage, phase current and back-EMF vectors while the $[R]$ and $[L]$ quantities are the matrices of the phase resistance and self- and mutual-inductances, respectively. The mechanical model is described by:

$$T_{em} + T_{cogg} + T_{reluct} = p[\Phi_0]^t[i] = J\frac{d\Omega}{dt} + f\Omega + T_{load} \tag{8}$$

where $p = 10$ is pole pair number, T_{em} is electromagnetic torque, T_{cogg} is the cogging torque and T_{reluct} is the reluctance torque. For the SFPMMs, their average reluctance torques are negligible under healthy conditions but can play a non-negligible role during short-circuit operations [30]. In the

model, the $[R]$, $[e_0]$ and T_{cogg} are considered as temperature dependent.

REFERENCES

[1] P. H. Mellor, D. Roberts and D. R. Turner, "Lumped parameter thermal model for electrical machines of TEFC design," *IEE Proceedings B - Electric Power Applications,* vol. 138, no. 5, pp. 205 - 218, Sept. 1991.

[2] G. Zhang, W. Hua, M. Cheng and J. Liao, "Design and comparison of two six-phase hybrid-excited flux-switching machines for EV/HEV applications," *IEEE Trans. Ind. Electron.,* vol. 63, no. 1, pp. 481-493, Jan. 2016.

[3] T. Raminosoa, G. Gerada and M. Galea, "Design considerations for a fault-tolerant flux-switching permanent-magnet machine," *IEEE Trans. Ind. Electron.,* vol. 58, no. 7, pp. 2818-2825, July 2011.

[4] Y. Shi, L. Jian, J. Wei, Z. Shao, W. Li and C. C. Chan, "A new perspective on the operating principle of flux-switching permanent-magnet machines," *IEEE Trans. Ind. Electron.,* vol. 63, no. 3, pp. 1425-1437, Mar. 2016.

[5] P. E. Kakosimos, A. G. Sarigiannidis, M. E. Beniakar, A. G. Kladas and C. Gerada, "Induction motors versus permanent-magnet actuators for aerospace applications," *IEEE Trans. Ind. Electron.,* vol. 61, no. 8, pp. 4315-4325, Aug. 2014.

[6] A. Fasolo, L. Alberti and N. Bianchi, "Performance comparison between switching-flux and IPM machine with rare earth and ferrite PMs," in *Proc. ICEM*, Marseille, France, 2-5 Sept. 2012.

[7] W. Hua, M. Cheng, Z. Q. Zhu and W. X. Zhao, "Comparison of electromagnetic performance of brushless machiness having magnets in stator and rotor," *J. Appl. Phys.,* vol. 103, no. 7, Mar. 2008.

[8] G. Zhao, L. Tian, Q. Shen and R. Tang, "Demagnetization analysis of permanent magnet synchronous machines under short circuit fault," in *Proc. of APPEEC 2010*, Chengdu, 28-31 Mar. 2010.

[9] S. Ruoho, J. Kolehmainen, J. Ikäheimo and A. Arkkio, "Interdependence of demagnetization, loading, and temperature rise in a permanent-magnet synchronous motor," *IEEE Trans. Magn.,* vol. 46, no. 3, pp. 949-953, Mar. 2010.

[10] P. Zhou, D. Lin, Y. Xiao, N. Lambert and M. A. Rahman, "Temperature-dependent demagnetization model of permanent magnets for finite element analysis," *IEEE Trans. Magn.,* vol. 48, no. 2, pp. 1031-1034, Feb. 2012.

[11] J. D. McFarland, T. M. Jahns and A. M. EL-Refaie, "Demagnetization performance characteristics of flux switching permanent magnet machines," in *Proc. ICEM2014*, Berlin, Germany, 2-5 Sept. 2014.

[12] S. Li, Y. Li and B. Sarlioglu, "Partial irreversible demagnetization assessment of flux switching permanent magnet machine using ferrite permanent magnet material," *IEEE Trans. Magn.,* vol. 51, no. 7, pp. 1-9, July July 2015.

[13] S. Zhu, M. Cheng, W. Hua and X. Cai, "Finite element analysis of flux-switching PM machine considering oversaturation and irreversible demagnetization," *IEEE Trans. Magn.,* vol. 51, no. 11, pp. 1-4, Nov. 2015.

[14] I. A. A. Afinowi, Z. Q. Zhu, Y. Guan, J. C. Mipo and P. Farah, "Performance analysis of switched-flux machines with hybrid NdFeB and ferrite magnets," in *Proc. of ICEMS 2014*, Hangzhou, 22-25 Oct. 2014.

[15] P. Taras, G. J. Li and Z. Q. Zhu, "Comparative study of fault tolerant switched flux permanent magnet machines," *IEEE Trans. Ind. Electron.,* vol. 64, no. 3, pp. 1939-1948, Mar. 2017.

[16] G. J. Li, P. Taras, Z. Q. Zhu, J. Ojeda and M. Gabsi, "Investigation of irreversible demagnetisation in switched flux permanent magnet machines under short-circuit conditions," *IET Electric Power Applications,* vol. 11, no. 4, pp. 595 - 602, April 2017.

[17] A. S. Thomas, Z. Q. Zhu and G. J. Li, "Thermal modelling of switched flux permanent magnet machines," in *Proc. ICEM*, Berlin, 2014.

[18] X. Cai, M. Cheng, S. Zhu and J. Zhang, "Thermal modelling of flux-switching permanent-magnet machines considering anisotropic conductivity and thermal contact resistance," *IEEE Trans. Ind. Electron.,* vol. 63, no. 6, pp. 3355-3365, June 2016.

[19] G. Zhang, W. Hua, M. Cheng, B. Zhang and X. Guo, "Coupled magnetic-thermal fields analysis of water cooling flux-switching permanent magnet motors by an axially segmented model," *IEEE Trans. Magn.,* vol. 53, no. 6, pp. 1-4, June 2017.

[20] G. J. Li, J. Ojeda, E. Hoang and M. Gabsi, "Thermal-electromagnetic analysis of a fault-tolerant dual-star flux-switching permanent magnet motor for critical applications," *IET Electrical Power Applications,* vol. 5, no. 6, pp. 503-513, July 2011.

[21] D. M. Ionel, M. Popescu, M. I. McGilp, T. J. E. Miller, S. J. Dellinger and R. J. Heideman, "Computation of core losses in electrical machines using improved models for laminated steel," *IEEE Trans. Ind. Appl.,* vol. 43, no. 6, pp. 1554 - 1564, Nov./Dec. 2007.

[22] D. Staton, A. Boglietti and A. Cavagnino, "Solving the more difficult aspects of electric motor thermal analysis in small and medium size industrial induction motors," *IEEE Trans. Energy Convers.,* vol. 20, no. 3, pp. 620-628, Sept. 2005.

[23] G. J. Li, J. Ojeda, E. Hoang and M. Gabsi, "Double and single layers flux-switching permanent magnet motors: Fault tolerant model for critical applications," in *ICEMS*, Beijing, 20-23 Aug. 2011.

[24] D. A. Staton and A. Cavagnino, "Convection heat transfer and flow calculations suitable for electric machines thermal models," *IEEE Trans. Ind. Electron.,* vol. 55, no. 10, pp. 3509-3516, Oct. 2008.

[25] J. H. Lienhard, A Heat Transfer Textbook, Cambridge, MA: Phlogiston Press, 2016.

[26] O. A. Mohammed, S. Liu and Z. Liu, "Physical modeling of PM synchronous motors for integrated coupling with machine drives," *IEEE Trans. Magn.,* vol. 41, no. 5, pp. 1628 - 1631, May 2005.

[27] B. Vaseghi, B. Nahid-Mobarakh, N. Takorabet and F. Meibody-Tabar, "Inductance identification and study of PM motor with winding turn short circuit fault," *IEEE Trans. Magn.,* vol. 47, no. 5, pp. 978-981, May 2011.

[28] L. Romeral, J. C. Urresty, J. R. Riba Ruiz and A. Garcia Espinosa, "Modeling of surface-mounted permanent magnet synchronous motors with stator winding interturn faults," *IEEE Trans. Ind. Electron.,* vol. 58, no. 5, pp. 1576-1585, May 2011.

[29] N. Leboeuf, T. Boileau, B. Nahid-Mobarakeh, N. Takorabet, F. Meibody-Tabar and G. Clerc, "Effects of imperfect manufacturing process on electromagnetic performance and online interturn fault detection in PMSMs," *IEEE Trans. Ind. Electron.,* vol. 62, no. 6, pp. 3388-3398, June 2015.

[30] E. Ben Sedrine, J. Ojeda, M. Gabsi and I. Slama-Belkhodja, "Fault-tolerant control using the GA optimization considering the reluctance torque of a five-phase flux switching machine," *IEEE Trans. Energy Convers.,* vol. 30, no. 3, pp. 927-938, Sept. 2015.